Electronic Supplementary Material (ESI) for Materials Horizons.

Supporting Information

Assembly of Hollow Mesoporous Nanoarchitectures Composed of Ultrafine Mo_2C Nanoparticles on N-doped Carbon Nanosheets for Efficient Electrocatalytic Reduction of Oxygen

Yanna Guo[a,b], Jing Tang[a]*, Joel Henzie[a], Bo Jiang[a], Huayu Qian[c], Zhongli Wang[a],
Haibo Tan[a,b], Yoshio Bando[a], and Yusuke Yamauchi[a,b,d,e]*

[a] International Center for Materials Nanoarchitectonics (MANA), National Institute for Materials Science (NIMS), 1-1 Namiki, Tsukuba, Ibaraki 305-0044, Japan.

E-mail: TANG.Jing@nims.go.jp

[b] Faculty of Science and Engineering, Waseda University, 3-4-1 Okubo, Shinjuku, Tokyo 169-8555, Japan

[c] Key Laboratory for Soft Chemistry and Functional Materials of Ministry Education, Nanjing University of Science and Technology, 210094, Nanjing, China.

[d] Australian Institute for Innovative Materials (AIIM), University of Wollongong, North Wollongong, NSW 2500, Australia. E-mail: yusuke@uow.edu.au

[e] School of Chemical Engineering & Australian Institute for Bioengineering and Nanotechnology (AIBN), The University of Queensland, Brisbane, QLD 4072, Australia

Experiment Section

Chemicals. Ammonium molybdate tetrahydrate ($(NH_4)_6Mo_7O_{24}\cdot 4H_2O$), dopamine hydrochloride (DA) and Nafion solution (5 wt %) were purchased from Sigma-Aldrich Chemical Co. Polystyrene-*b*-poly(ethylene oxide) (PS_{173}-*b*-PEO_{170}) was purchased from Polymer Source Inc. Ammonia hydroxide ($NH_3\cdot H_2O$), absolute ethanol, potassium hydroxide (KOH) and tetrahydrofuran (THF) were purchased from Wako Co. All the chemicals were used without further purification.

Preparation of hollow mesoporous nanoarchitectures composed of ultrafine Mo_2C nanoparticles on N-doped carbon nanosheets (MMo_2C/NCS). The typical synthetic process is as follows. Dopamine hydrochloride (25 mg) was dissolved in a mixed solvent of ethanol and deionized water (volume ratio is 1:2, 3 mL in total) to generate the clear solution A. Ammonium molybdate tetrahydrate (100 mg) was dissolved in deionized water (4 mL) to prepare solution B. Then solution A was added into 2 mL of THF containing 15 mg of diblock copolymer PS_{173}-*b*-PEO_{170} under mild stirring. After 5 minutes, solution B was added into the mixture under stirring and the color of reaction system changed from transparent to orange. After stirring another 5 min, 0.5 mL of aqueous ammonia aqueous solution (NH_4OH, 28-30%) was injected into the reaction to initiate self-polymerization of dopamine and causing the color of the solution became orange-red. After continuous reaction for 8 hours, the precipitates were washed via several rinsing-centrifugation cycles with de-ionized water and ethanol and then dried at 60 °C for 12 hours. All synthetic experiments were carried out at room temperature (*ca.* 22 °C). The synthesis process of precursor Mo-PDA-PS was summarized in **Table S1**. For carbonization, the above precipitates were pre-heated at 350 °C for 2 hours and finally heated at 900 ^{o}C for 1 hour under nitrogen atmospheres with a heating rate of 5 °C min^{-1} to generate the MMo_2C/NCS structures.

For comparison, additional samples were prepared to obtain some insights into the relationships between structures and electrocatalytic activity. Mesoporous carbon spheres were prepared according to our group's previous report.[S1] Hollow spherical Mo_2C/N-doped carbon (Mo_2C/NCS) were obtained through the similar synthetic process with Mo_2C/NCS except that PS_{173}-*b*-PEO_{170} was not used in the synthesis of precursor (Mo-PDA).

To investigate the impact of Mo_2C content on the catalytic performance, another two samples were also prepared through changing the ammonium molybdate tetrahydrate concentration in the reaction system. One of the samples is prepared by using lower concentration of molybdate, the obtained precursor is named as Mo-PDA-PS-low. After carbonization, the sample is abbreviated as MMo_2C/NCS-low. The other one is prepared by using a higher concentration of molybdate, the obtained precursor and the carbonized products are abbreviated as Mo-PDA-PS-high and MMo$_2$C/NCS-high, respectively. The synthetic processes are similar to the hollow MMo$_2$C/NCS heterostructures. For Mo-PDA-PS-low, ammonium molybdate tetrahydrate (50 mg) was added into the reaction system, while for Mo-PDA-PS-high, ammonium molybdate tetrahydrate (200 mg) was added into the reaction system.

Characterizations. Hitachi SU-8000 field-emission scanning electron microscopy (SEM) was used to observe the morphology of the samples at an accelerating voltage of 5 kV. Transmission electron microscopy (TEM) and elemental mapping analysis were performed to investigate the inner structures of the samples using a JEM-2100F operated at 200 kV. X-ray diffraction (XRD) patterns were characterized on a Rigaku RINT 2000X-ray diffractometer with monochromated Cu Kα radiation (40 kV, 40 mA) at a scanning rate of 1 $°C \cdot min^{-1}$. Raman spectra were assessed by Horiba-Jovin Yvon T64000 with the excitation Laser of 364 nm. Nitrogen adsorption-desorption isotherms were acquired by using a BELSORP-mini (BEL, Japan) at 77 K to estimate the surface areas based on Multipoint Brunauer-Emmett-Teller (BET) method. The total pore volumes and pore size distributions were calculated from the adsorption branches of isotherms based on the Barrett-Joyner-Halenda (BJH) model. X-ray photoelectronic spectroscopy (XPS) spectra were carried out by using a PHI Quantera SXM (ULVAC-PHI) instrument with an Al Kα X-ray source. All the binding energies were calibrated using the C 1s peak as a reference (285.0 eV). Thermal gravity (TG) analysis was obtained by using a Hitachi HT-Seiko Instrument Exter 6300 TG/DTA. The UV adsorption spectra were measured using a JASCO V-570 UV-vis-NIR spectrophotometer. Fourier transform infrared spectroscopic (FTIR) measurements were recorded on a thermoscientific Nicolet 4700 using KBr pellets. Zeta-potential measurement was checked using a beckman particle size and zeta potential analyzer. Inductively coupled plasma optical emission spectroscopy (ICP-OES) was used to check the content of Mo element by using a Hitachi model SPS3520UV-DD.

Electrochemical measurements. Electrochemical testing was performed in a three-electrode system, with rotating disk as the working electrode, Ag/AgCl (3M) as the reference electrode, and Pt wire as the counter electrode under room temperature. The working electrode was prepared as follows. Typically, 2 mg of catalyst was dispersed in 400 μL of 1:3 (v/v) isopropanol/water mixed solvent with 20 μL Nafion solution (5 wt%). Mixing was assisted by sonication for 1 h to form a homogenous catalyst ink. Then 5 μL of the above suspension was dropped on the polished glassy carbon (GC) electrode with 4 mm diameter (RRDE Pt Ring/GC Disk Electrode, cat. NO. 011162, ALS Co., Ltd.), and dried at room temperature. The loading of the catalyst was 0.2 mg cm^{-2}. The electrochemical measurements were performed in O_2/N_2 saturated 0.1 M KOH electrolytes and the flow of O_2/N_2 was maintained over the electrolyte during the test. The polarization curves for ORR were carried out by the rotating disk electrode (RDE) or a rotating ring-disk electrode (RRDE) technique. RDE measurements were conducted by liner sweep voltammetry (LSV). The disk electrode was scanned at a rate of 10 mV s^{-1} and rotating speed of 1600 rpm at potential between 0.2 and 1.2 V (*vs.* RHE), and the ring electrode potential was held at 1.2 V(*vs.* RHE). All the CV measurements were conducted at a scan rate of 50 mV s^{-1} from -0.036 to 1.164 V (*vs.* RHE). The durability test of the catalysts were carried out using the accelerated durability test protocol by cycling the catalysts between 0.6 and 1.0 V (*vs.* RHE) at a scan rate of 50 mV s^{-1} in O_2-saturated 0.1 M KOH solution. The current densities are normalized to the geometric area (0.1256 cm^2) of the glassy carbon disk. In order to gain insight to the kinetics of ORR on mesoporous Mo_2C/N-doped carbon, RDE measurements was conducted under different rotation rate from 400 to 2500 rpm with a scan rate of 10 mV s^{-1}. Electron transfer numbers were calculated using the Koutecky–Levich equation:

$$\frac{1}{j} = \frac{1}{j_L} + \frac{1}{j_K} \quad (1)$$

$$j_L = B\omega^{1/2} = 0.62nFC_0(D_0)^{2/3}\upsilon^{-1/6}\,\omega^{1/2} \quad (2)$$

Where, ω is the angular velocity, j is the measured current density, j_K and j_L are the kinetic and diffusion-limiting current densities, respectively, n is the number of transferred electron in oxygen reduction, F is the Faraday constant (96485 C mol^{-1}), C_0 is the bulk concentration of O_2 (1.2×10^{-6} mol cm^{-3}), D_0 is the diffusion coefficient of O_2 (1.9×10^{-5} cm^2 s^{-1}), and υ is the kinematic viscosity of the electrolyte (0.01 cm^2 s^{-1}). B can be derived from the slope of the K-L equation.

To obtain in-depth understanding on the ORR process, RRDE voltammograms were also measured. The electron transfer number (n) per oxygen molecule was calculated from RRDE voltammograms according to the following equation.

The following equations were used to calculate the number of transferred electron (n), respectively:

$$n = \frac{4I_D}{I_D + (I_R/N)} \quad (3)$$

Where, where I_D is the disk current, I_R is the ring current.

Figure S1

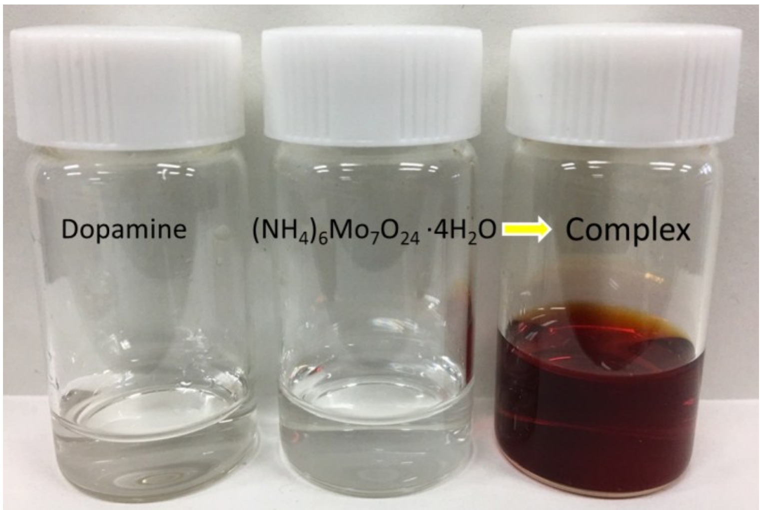

Figure S1. Photo image of dopamine, $(NH_4)_6Mo_7O_{24}\cdot 4H_2O$ solutions, and their mixed solution MoO_4^{2-}/DA.

Figure S2

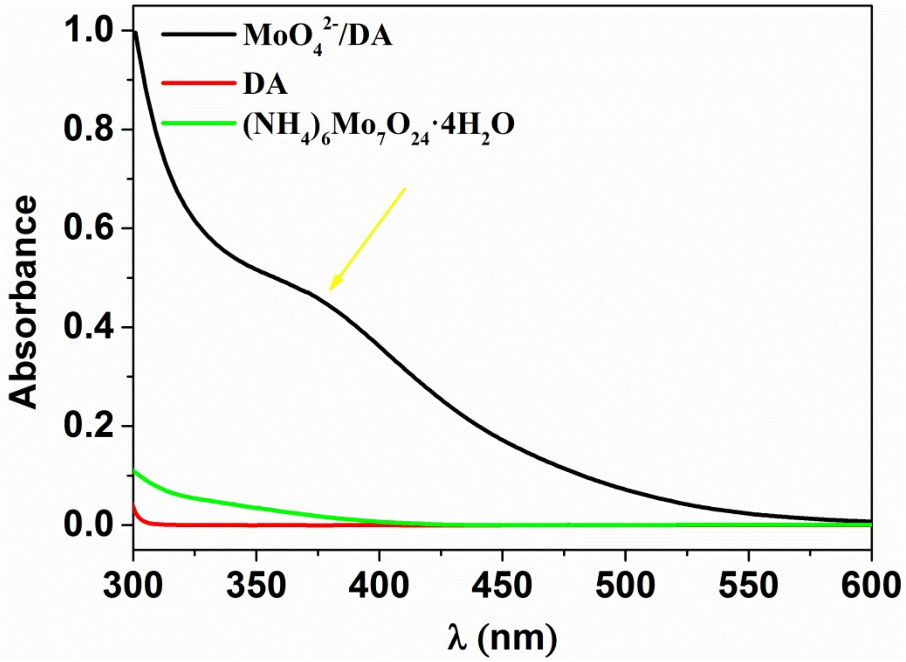

Figure S2. UV absorption spectra of DA, $(NH_4)_6Mo_7O_{24}\cdot 4H_2O$ solutions, and their mixed solution MoO_4^{2-}/DA.

Figure S3

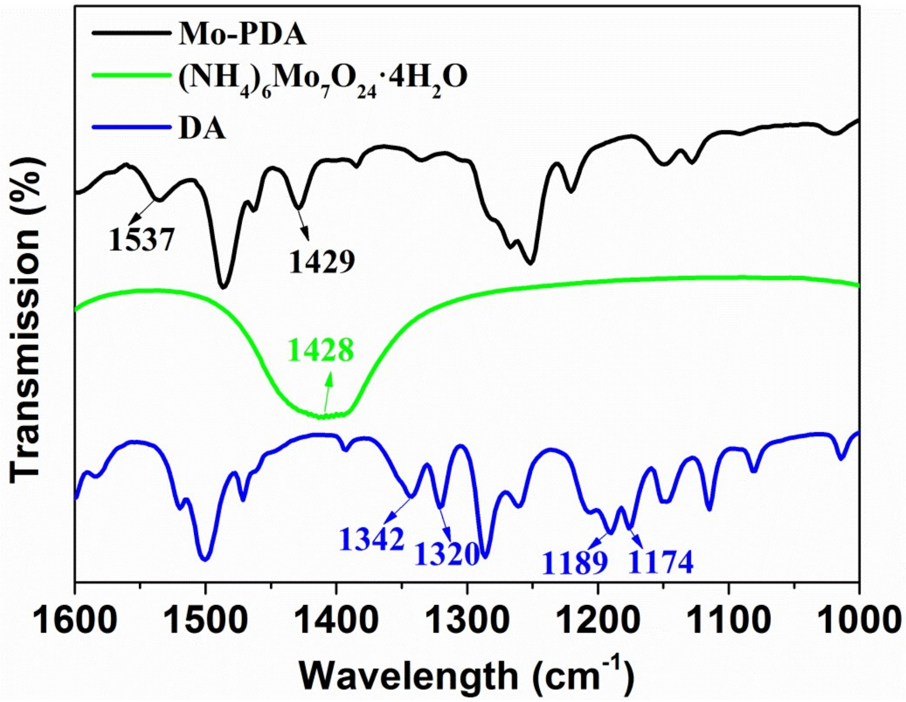

Figure S3. FTIR spectra of DA, $(NH_4)_6Mo_7O_{24}\cdot 4H_2O$, and the product of Mo-PDA formed by the polymerization of MoO_4^{2-}/DA complex in the alkaline environment.

Figure S4

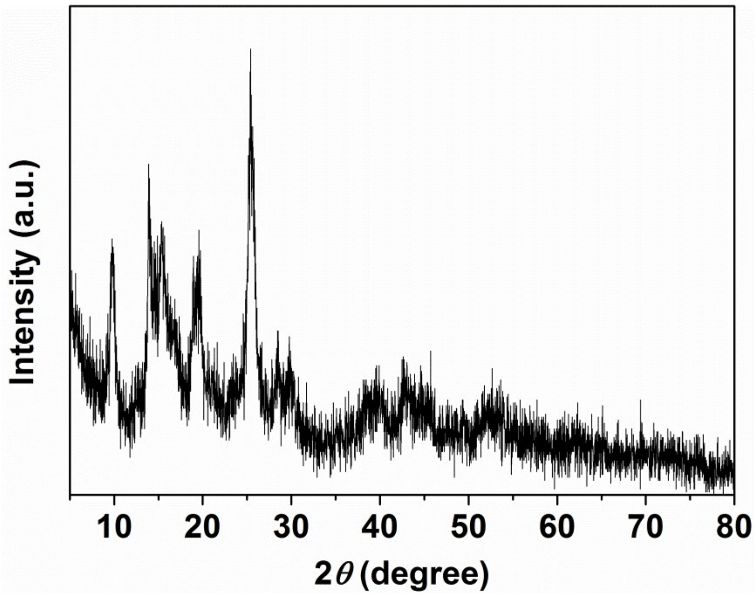

Figure S4. XRD pattern of the as-prepared Mo-PDA-PS precursor.

Figure S5

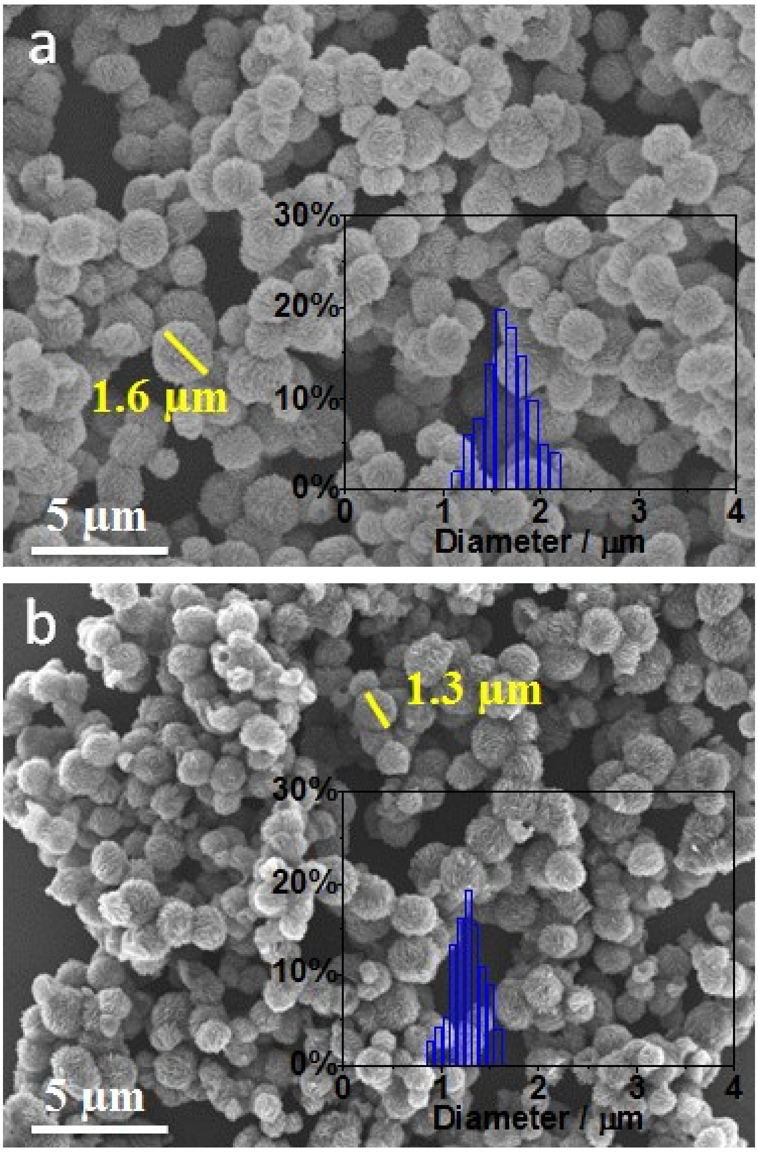

Figure S5. SEM images of samples before and after carbonization. (a) Mo-PDA-PS precursor, and (b) MMo_2C/NCS. Insets are the particle size distribution diagrams.

Figure S6

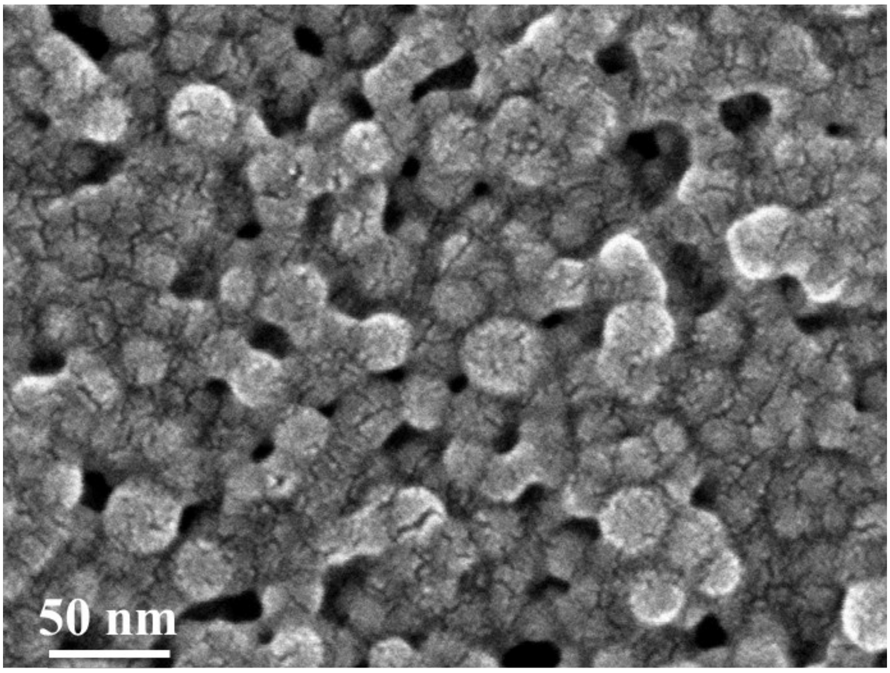

Figure S6. SEM image of PS_{173}-*b*-PEO_{170} micelles dispersed in a 9 mL of mixed solution containing THF, water, and ethanol with volume ratio of 2:6:1.

Figure S7

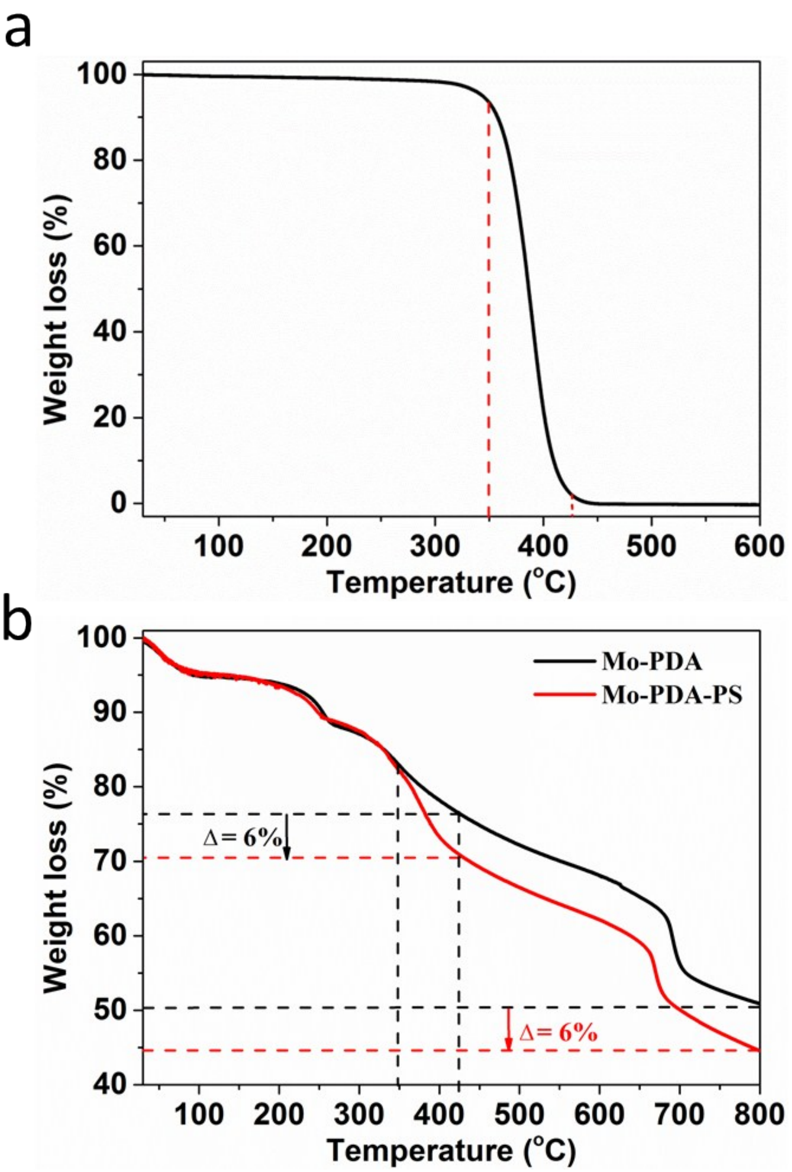

Figure S7. TG curves of (a) PS-*b*-PEO, and (b) Mo-PDA and Mo-PDA-PS measured in N_2 atmosphere.

Figure S8

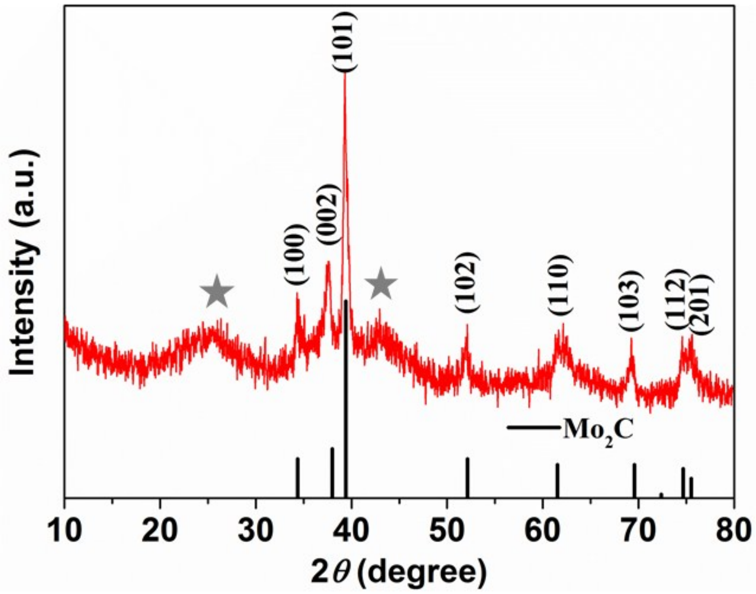

Figure S8. XRD pattern of the as-prepared MMo$_2$C/NCS.

Figure S9

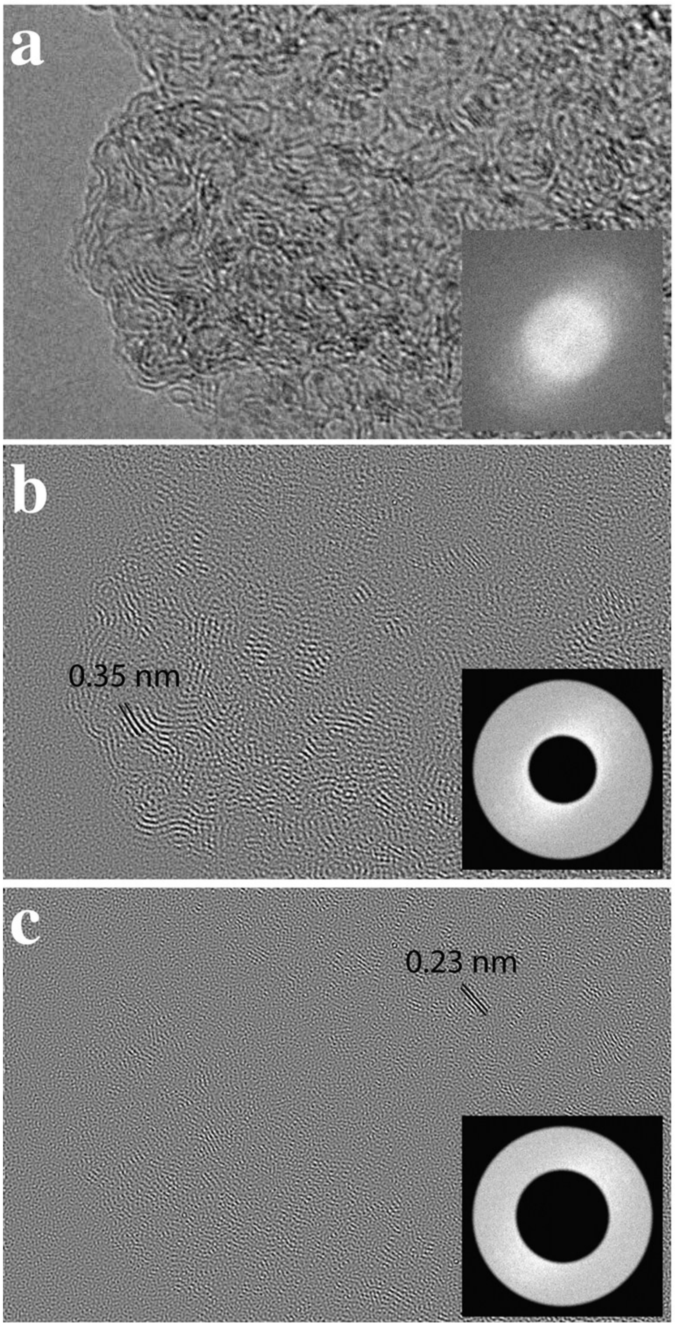

Figure S9. (a) HRTEM image of the hollow spherical MMo$_2$C/NCS particles. The FFT of the entire image (Inset) shows some structures indicative of a periodic lattice fringes with random orientations. (b) An annular bandpass filter was applied to the FFT image (Inset) and then a reverse FFT was applied to reconstruct the image. Lattice fringes match with the spacing of carbon nanosheets. (c) An annulus with a slightly larger central diameter (Inset) was applied to filter out carbon. The lattice fringes from Mo$_2$C nanocrystallites are easily observed.

Figure S10

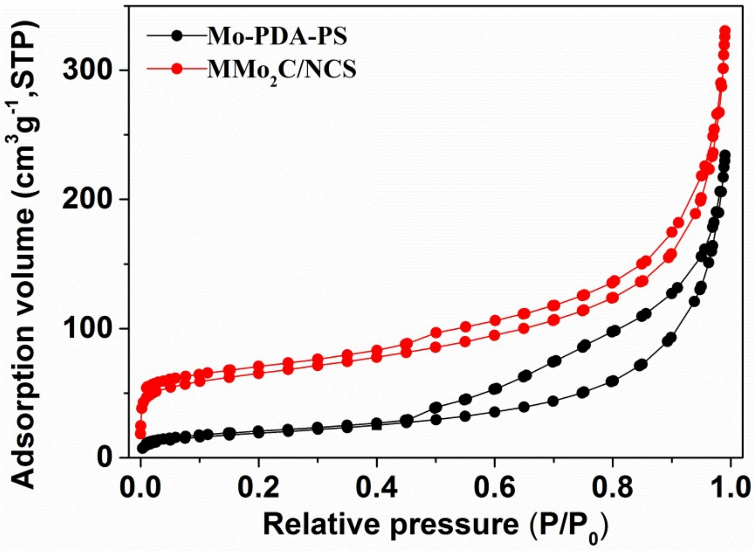

Figure S10. N_2 adsorption-desorption isotherms of Mo-PDA-PS precursor and MMo$_2$C/NCS.

Figure S11

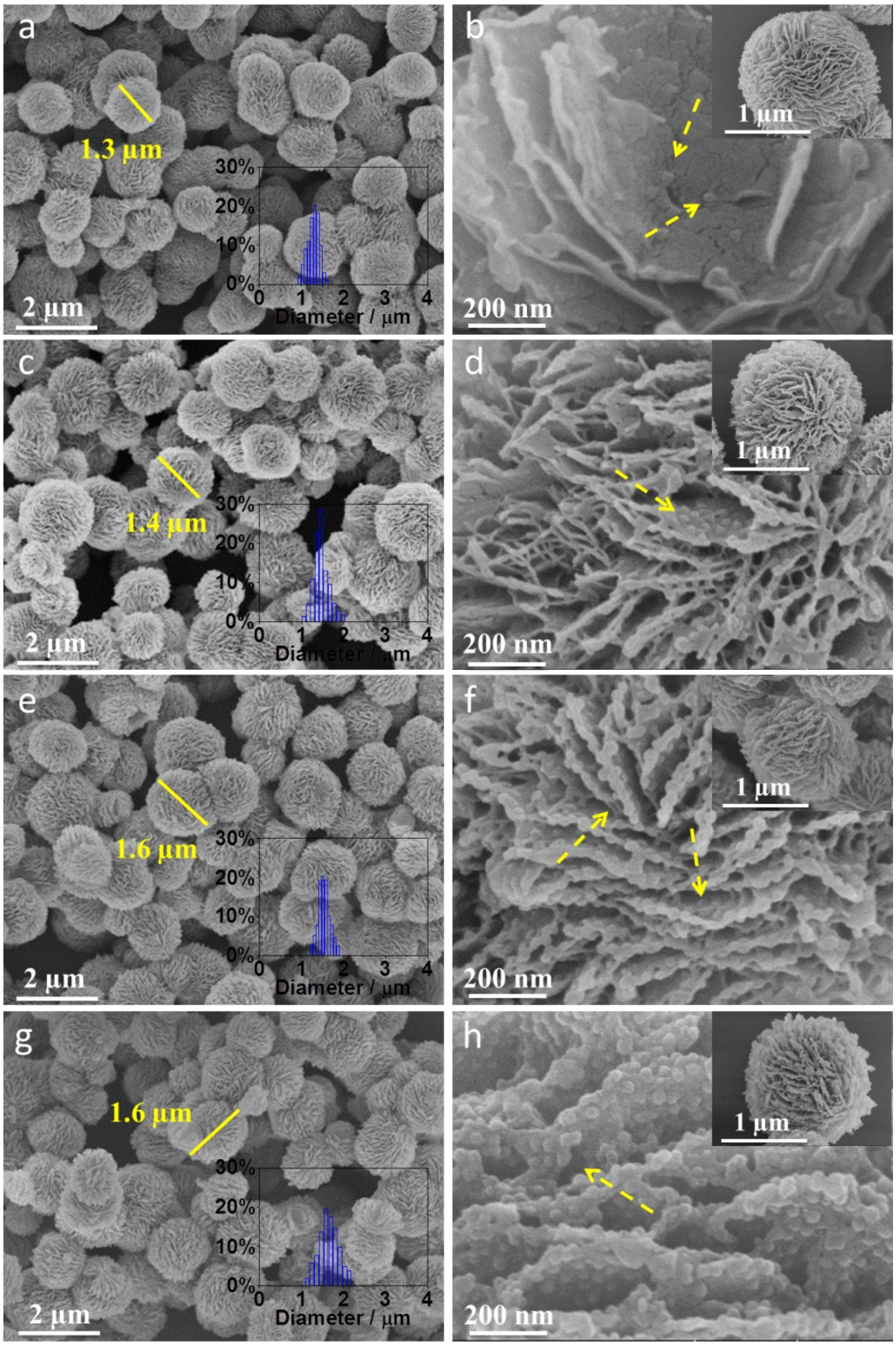

Figure S11. Typical SEM images of products Mo-PDA-PS after reaction for a,b) 5 min, c,d) 30 min, e,f) 4 hours, and g,h) 8 hours.

Figure S12

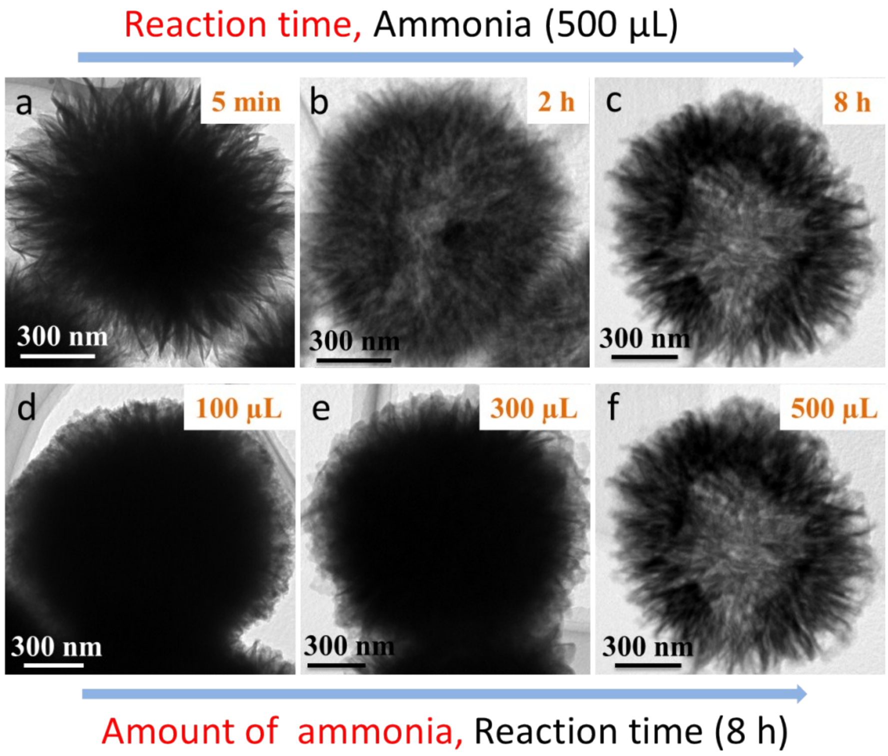

Figure S12. TEM images of the Mo-PDA-PS precursor obtained after reaction for (a) 5 min, (b) 2 hours, and (c) 8 hours when the amount of ammonia is fixed as 500 μL. TEM images of Mo-PDA-PS obtained after reaction for 8 h with ammonia of (d) 100 μL, (e) 300 μL, and (f) 500 μL.

Figure S13

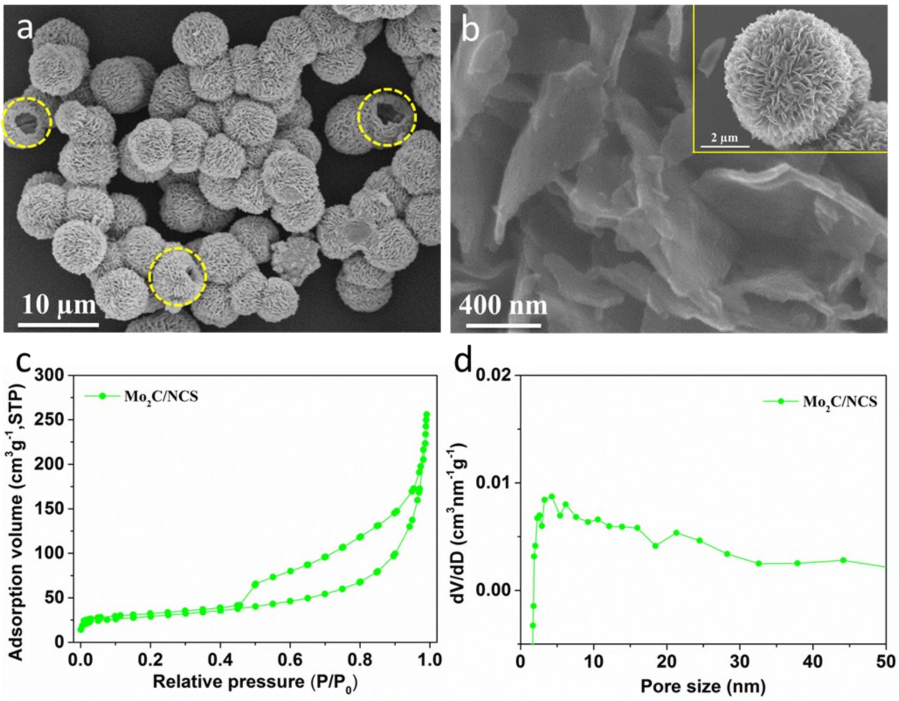

Figure S13. (a,b) SEM images, (c) N_2 adsorption-desorption isotherms, and (d) corresponding pore size distribution of Mo_2C/NCS. Inset in (b) is the SEM image of a single particle of Mo_2C/NCS.

Figure S14

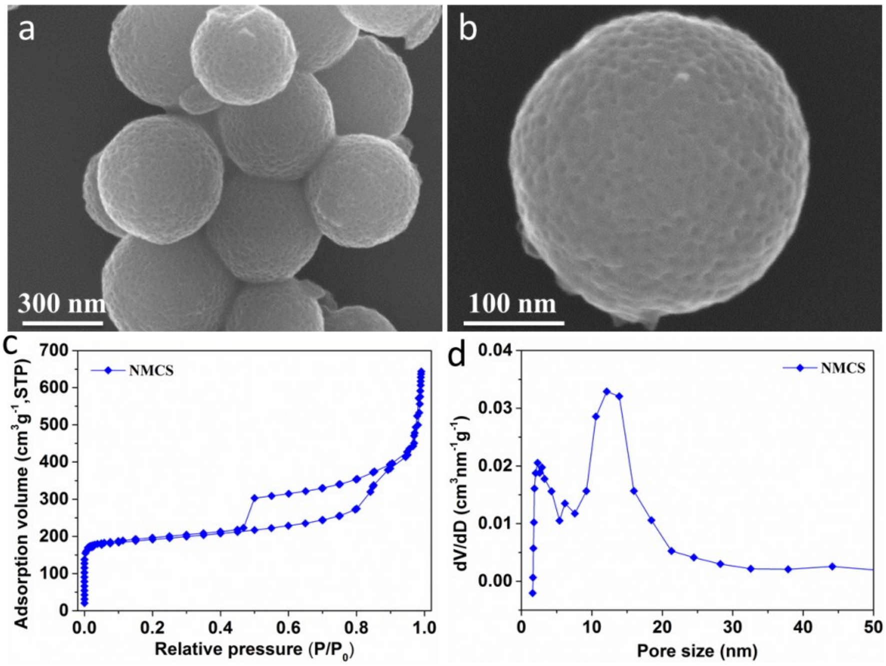

Figure S14. (a,b) SEM images, (c) N_2 adsorption-desorption isotherms, and (d) corresponding pore size distribution of NMCS.

Note in Figure S13 and Figure S14: As shown in **Figure S13a-b,** Mo_2C/NCS reveals a hollow sphere structure which can be seen from some cracked particles, and the spheres are organized by smooth nanosheets with size of ~5 µm. This structure of Mo_2C/NCS leads to a relatively low surface area of 96 m^2 g^{-1} due to the absence of mesopores in the nanosheets (**Figure S13c-d**). NMCS has a spherical structure with a diameter of ~300 nm as shown in **Figure S14a,b**, and abundant mesopores with size of ~15 nm distributed throughout the whole sphere. The specific surface area of NMCS is as high as 575 m^2 g^{-1} (**Figure S14c-d**).

Figure S15

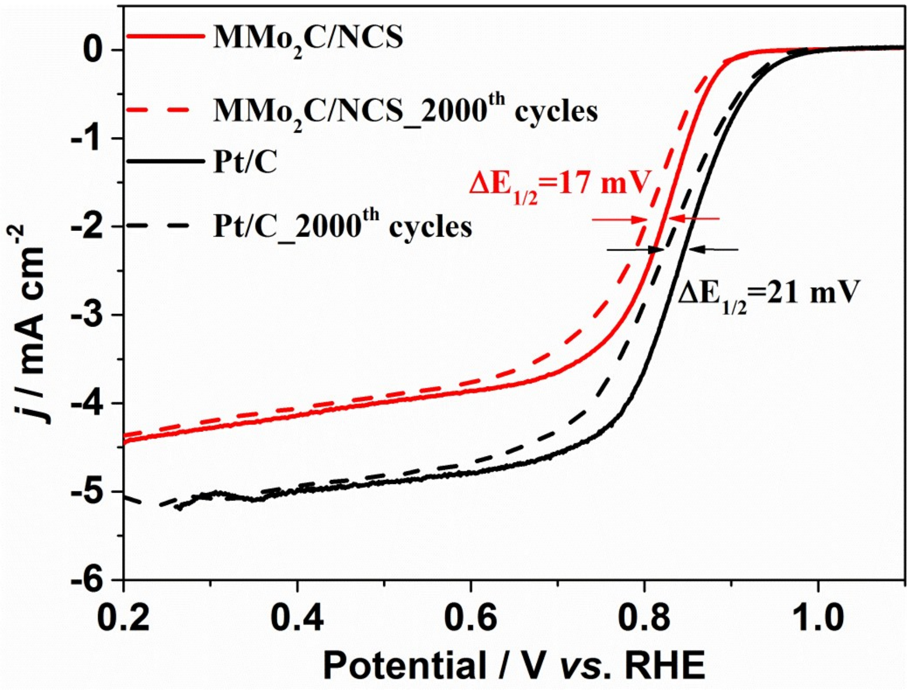

Figure S15. LSV curves of hollow spherical MMo_2C/NCS and Pt/C obtained from the first and the 2000th cycle in 0.1 M KOH.

Figure S16

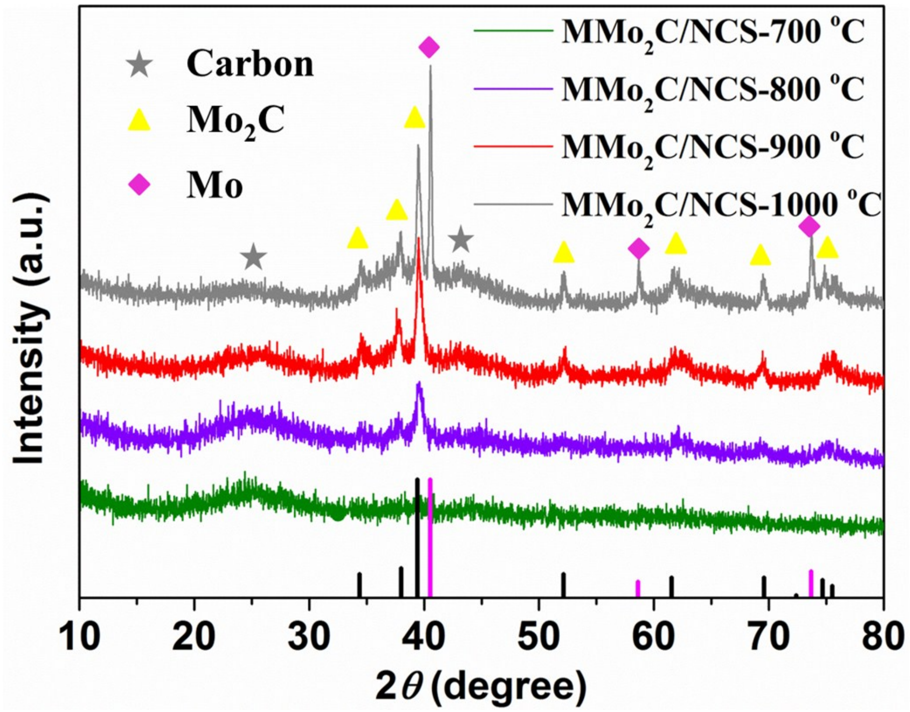

Figure S16. XRD patterns of the samples prepared by carbonization of the Mo-PDA-PS precursors (obtained after 8 hours reaction) at 700, 800, 900 and 1000 ºC.

Figure S17

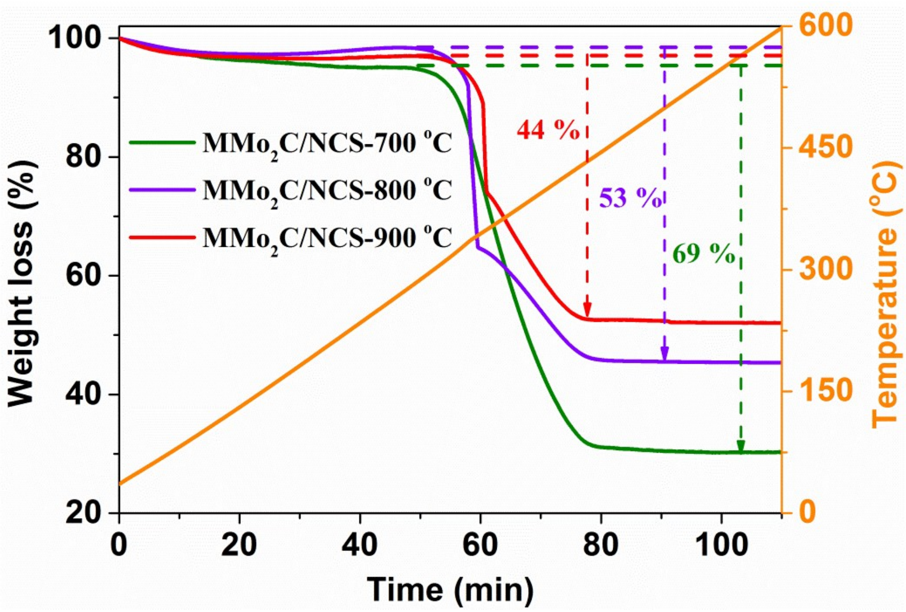

Figure S17. TG curves of the obtained hollow spherical MMo_2C/NCS-700 °C, MMo_2C/NCS-800 °C, and MMo_2C/NCS-900 °C samples measured under air atmosphere.

Note in Figure S17: As observed in **Figure S17**, all of the three samples reveal apparent decreases in the sample's weights over the temperature range of 300–450 °C. It is noteworthy that steep weight loss occurs for both MMo_2C/NCS-800 °C and MMo_2C/NCS-900 °C samples at the temperature before 325 °C and 400 °C, respectively. While MMo_2C/NCS-700 °C shows a gradual weight decrease with the increased temperature before 450 °C. Considering the composition of the samples, the weight loss processes in air mainly contain the combustion of N-doped carbon sheets, and the oxidization of Mo_2C nanoparticles to form MoO_3. For MMo_2C/NCS-700 °C sample, the bind force in Mo_2C was a bit weak, thus the combustion of N-doped carbon (weight loss process) accompanied with the reaction between unstable Mo and O to form MoO_3 (weight increase process) at the temperature from 300 to 450 °C, resulting in a gradual weight decrease of MMo_2C/NCS-700 °C and a relative smooth TG curve. For MMo_2C/NCS-800 °C and MMo_2C/NCS-900 °C samples, Mo_2C nanoparticles were more stable than those in MMo_2C/NCS-700 °C due to the higher-temperature carbonization. Therefore, the carbon combustion started earlier than the oxidization of Mo_2C at the relative low temperature of 300–350°C. Thus a steep weight loss was observed in TG curves due to the only combustion of carbon. When the temperature increased higher than 350 °C, the oxidation of Mo_2C occurs and compensate the weight loss of carbon, thus the weight loss of MMo_2C/NCS-800 °C and MMo_2C/NCS-900 °C became slowly.

Figure S18

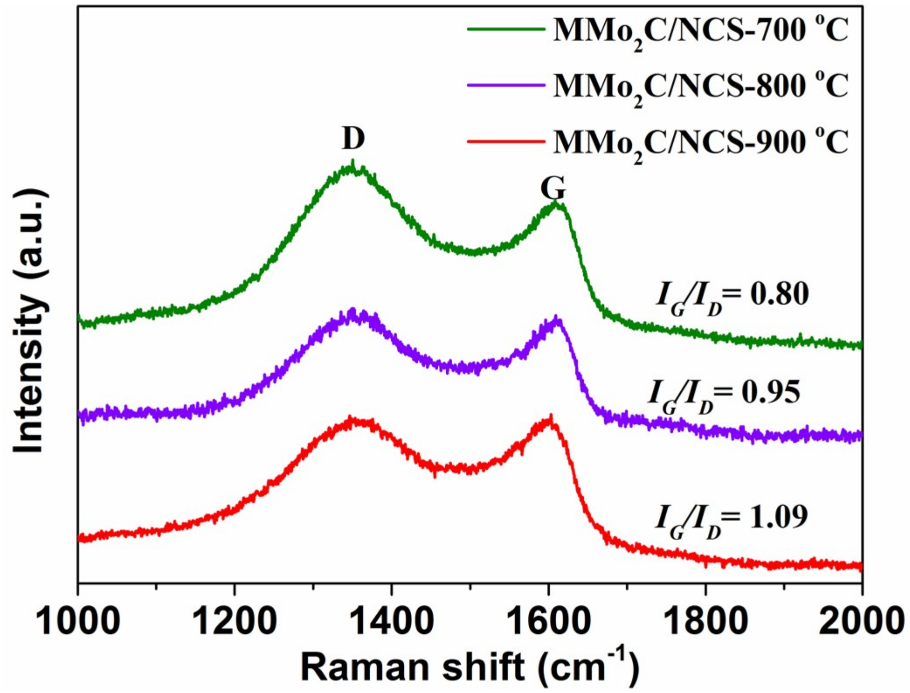

Figure S18. Raman spectrums of the MMo_2C/NCS-700 °C, MMo_2C/NCS-800 °C, and MMo_2C/NCS-900 °C samples.

Figure S19

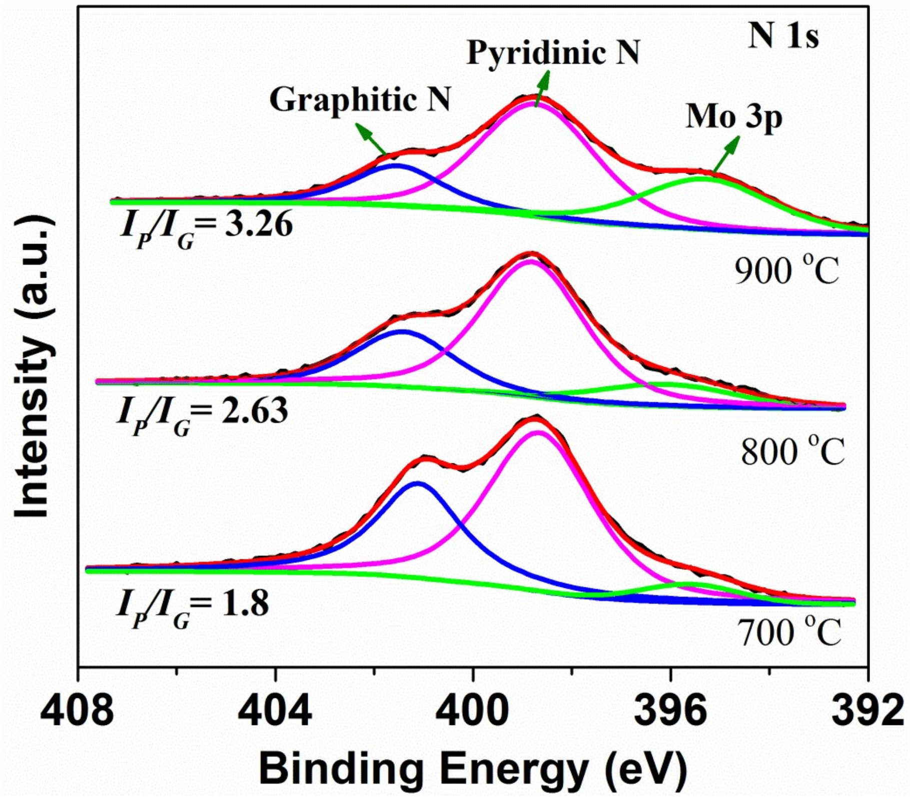

Figure S19. High-resolution N 1s XPS spectrums of the MMo_2C/NCS-700 °C, MMo_2C/NCS-800 °C, and MMo_2C/NCS-900 °C samples.

Figure S20

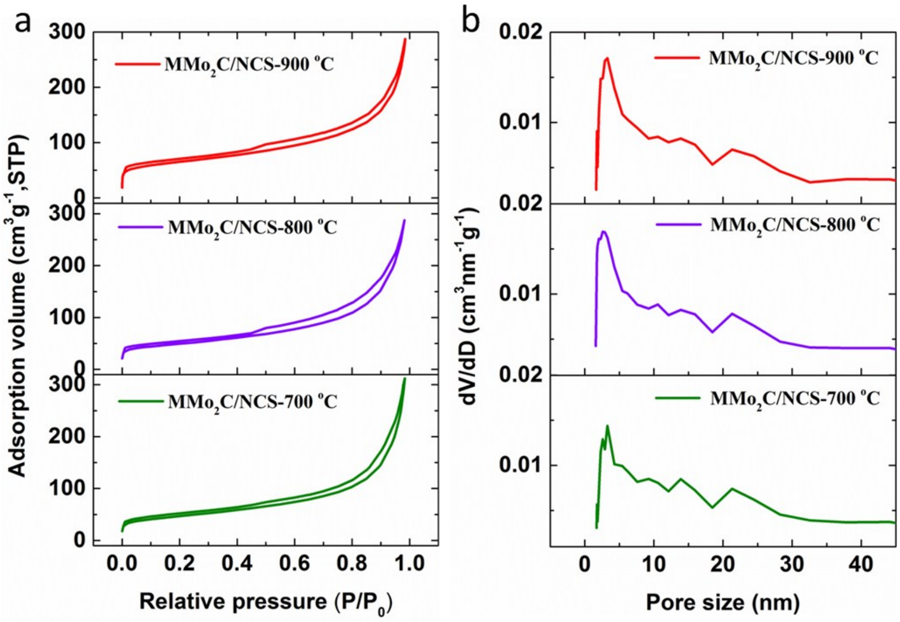

Figure S20. (a) N_2 adsorption-desorption isotherms, and (b) corresponding pore size distribution of hollow spherical MMo_2C/NCS samples carbonized at different temperatures.

Note in **Figure S20**: All of the samples show type IV isotherms with a hysteresis, indicating a high fraction of textural porosity (**Figure S20a**). The N_2 uptake at very low relative pressure (P/P_0 = 0-0.01) reveal the presence of micropores. The broad capillary condensation ranges from $P/P_0 \approx 0.43$ to almost $P/P_0 \approx 1$, indicating there are hierarchical mesopores and macropores. The micropores and macropores might derive from the pyrolysis of polydopamine and the open channel between the 2D nanosheets in MMo_2C/NCS, respectively.[S2] The mesopore size distributions were calculated by applying the BJH method. As shown in **Figure S20b**, all the samples have a wide pore size distribution, ranging between 2 and 35 nm. The mesopores are formed by the removal of the spherical block copolymer PS-*b*-PEO micelles, as well as the interspace between the packing nanosheets. The specific surface areas and pore volumes of MMo_2C/NCS-700 °C, MMo_2C/NCS-800 °C, and MMo_2C/NCS-900 °C are summarized in **Table S2**.

Notes in Figure S16-20: The Mo-PDA-PS precursors were carbonized at various temperatures from 700 to 900 °C and the physicochemical properties of the samples were investigated by XRD (**Figure S16**), Thermogravimetric analysis (TGA) (**Figure S17**), Raman spectra (**Figure S18**), XPS spectra (**Figure S19**), and N_2 adsorption-desorption isotherms (**Figure S20**). As seen in **Figure S16**, carbon is the main component and the peak of Mo_2C is almost negligible when the carbonization temperature is 700 °C, after increasing the temperature from 700 to 900 °C, the peak intensity of Mo_2C are gradually increased. TG analysis (**Figure S17**) of samples conducted in air further confirms the change of carbon and Mo_2C contents in the final products with the temperature increase. The totally weight loss of MMo_2C/NCS samples carbonized at 700 °C, 800 °C, and 900 °C are measured about 44%, 53%, and 69%, respectively, suggesting the Mo_2C contents in the hybrid materials are gradually increased at higher temperatures. Raman spectroscopy (**Figure S18**) was conducted to investigate the carbon state in all the samples. There are two peaks located at ~1350 cm^{-1} (D band) and 1600 cm^{-1} (G band), which correspond to the vibration of sp^3 carbons/defect and graphitic sp^2 carbons, respectively. The relative intensity ratio of G band to D band (I_G/I_D) increases from 0.8 to 1.09 along with the increased temperatures, indicating the enhanced graphitization of the carbon matrix. As it is known, the enhanced graphitic degree of the carbon matrix could improve the conductivity, which is beneficial for increasing the catalytic performance of electrode. [S3,S4] **Figure S19** shows the high resolution XPS spectrums of N 1s, the spectrum can be fitted into three peaks located at binding energies of 398.7 eV, 401.5 eV, and 395.3 eV, which are correspond to the pyridinic-N, graphitic-N, and Mo 3p, respectively. When the carbonization temperature increases from 700 to 900 °C, N concentration decreases from 6.9 atomic% to 4.7 atomic%, while the ratio of pyridinic-N to graphitic-N distinctly increases from 1.8 to 3.3. The specific surface area of MMo_2C/NCS increases from 165 m^2 g^{-1} at 700 °C, to 200 m^2 g^{-1} at 800 °C and 212 m^2 g^{-1} at 900 °C, which are attributed to the generation of more micropores at higher temperatures (**Figure S20**). The physicochemical properties and elemental compositions of MMo_2C/NCS after carbonization at various temperature (700, 800, and 900 °C) are described in **Table S2**.

Figure S21

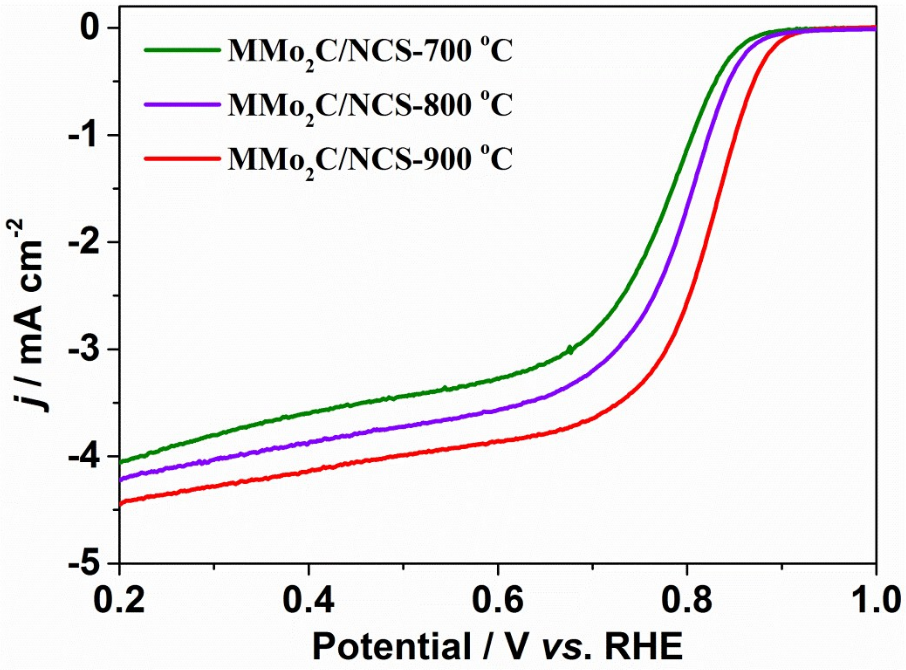

Figure S21. LSV curves of hollow spherical MMo$_2$C/NCS samples carbonized at different temperatures.

Figure S22

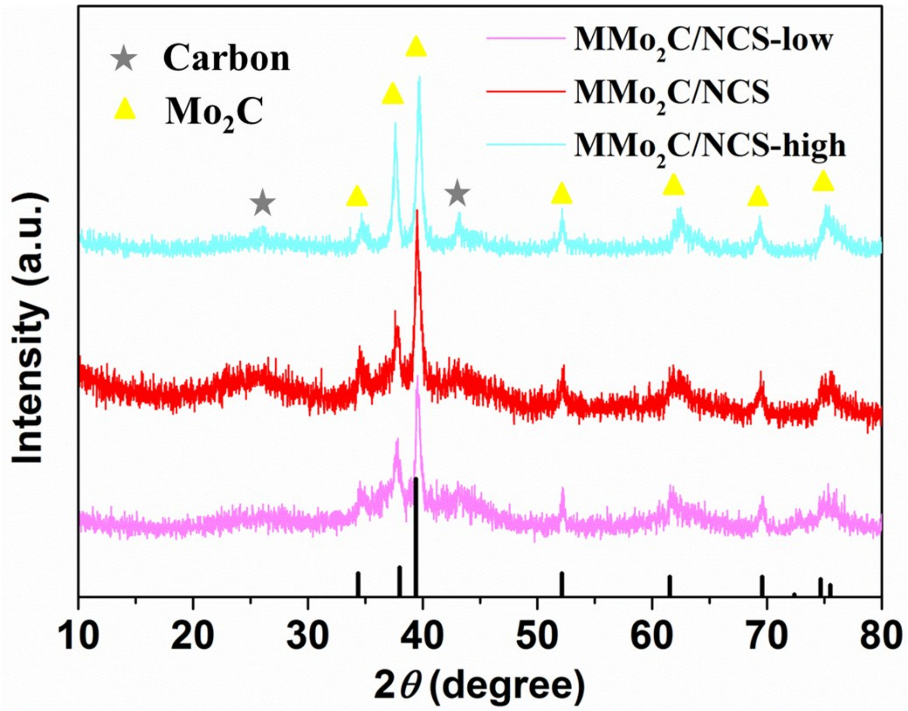

Figure S22. XRD patterns of the synthesized MMo_2C/NCS-low, MMo_2C/NCS and MMo_2C/NCS-high.

Note in Figure S22: The XRD patterns in **Figure S22** show that both MMo_2C/NCS-high and MMo_2C/NCS-low samples are composed of carbon and Mo_2C, which are consistent with MMo_2C/NCS.

Figure S23

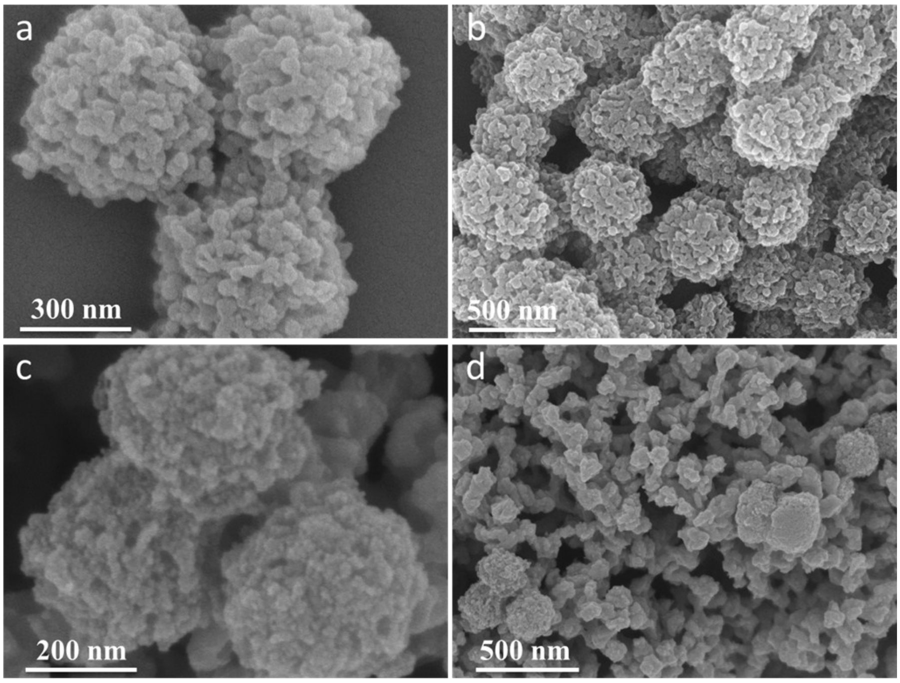

Figure S23. SEM images of (a, b) Mo-PDA-PS-low, and (c, d) MMo$_2$C/NCS-low.

Figure S24

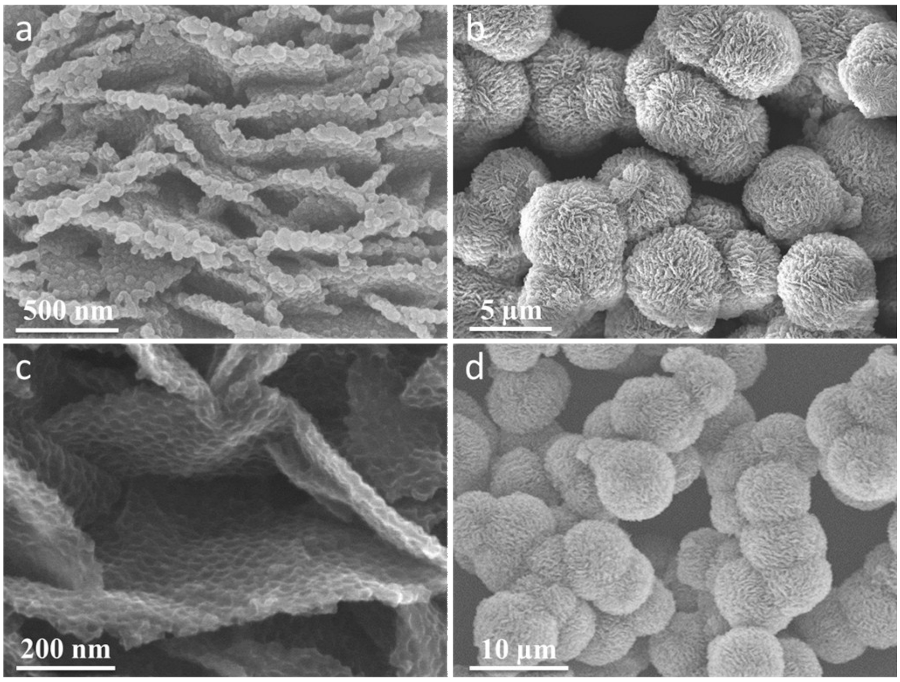

Figure S24. SEM images of (a,b) Mo-PDA-PS-high, and (c,d) MMo_2C/NCS-high.

Note in Figure S23 and Figure S24: As shown in **Figure S23a-b**, when the concentration of molybdate is decreased, the obtained Mo-PDA-PS-low precursor particles are spherical but smaller in diameter (~500 nm). After carbonizing the Mo-PDA-PS-low precursor at 900 °C for 1h under N_2 atmosphere, the MMo_2C/NCS-low sample exhibits an irregular morphology (**Figure S23c-d**). SEM micrographs in **Figure S24a-b** show that the Mo-PDA-PS-high precursor has a similar 3D microspherical structure to Mo-PDA-PS precursor, and the 3D microsphere is composed of PS-*b*-PEO spherical micelles on Mo-PDA nanosheets. However, the particle size is increased to ~6 μm. After carbonization, discrete mesopores can be seen on the surface of the nanosheets in the MMo_2C/NCS-high nanoparticles (**Figure S24c-d**).

Figure S25

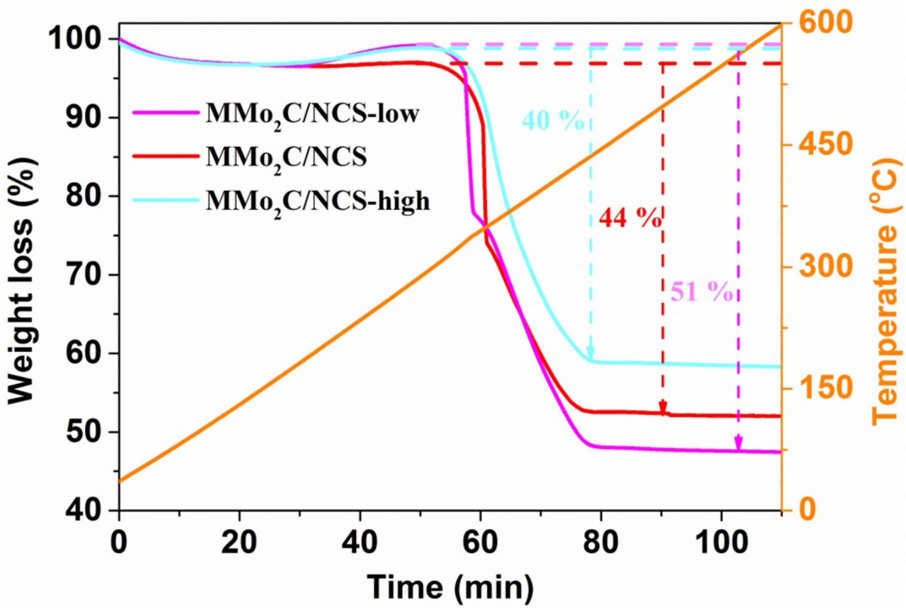

Figure S25. TG curves of the obtained MMo$_2$C/NCS-low, MMo$_2$C/NCS, and MMo$_2$C/NCS-high samples measured under air atmosphere.

Note in Figure S25: The weight losses occur for both MMo$_2$C/NCS-low and MMo$_2$C/NCS-high samples at the temperature below ~450 °C. The total weight loss of MMo$_2$C/NCS-high is about 40%, which is smaller than that of MMo$_2$C/NCS (44%) and MMo$_2$C/NCS-low (51%). This observation suggests that the Mo$_2$C concentration in the three samples gradually increases with higher concentrations of molybdate precursor.

Figure S26

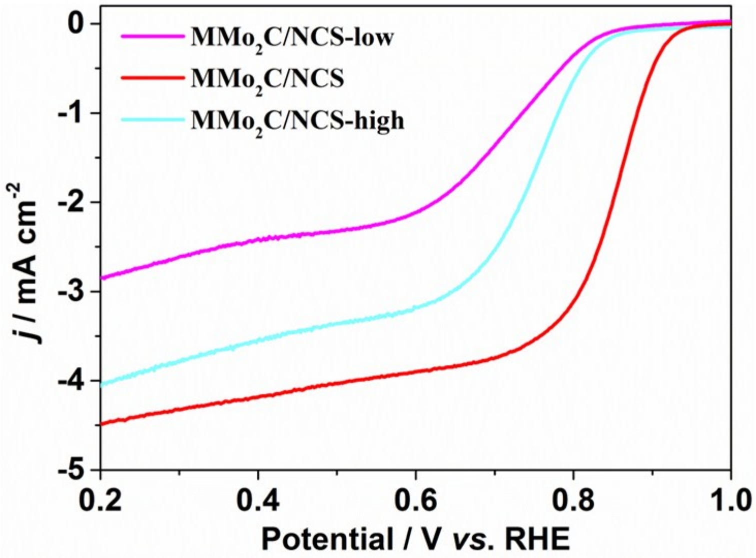

Figure S26. LSV curves of MMo$_2$C/NCS-low, MMo$_2$C/NCS, and MMo$_2$C/NCS-high.

Table S1. Synthesis parameters of Mo-PDA-PS spheres at room temperature.

Sample	PS-*b*-PEO / THF (mg) / (mL)		DA / Water & Ethanol (mg) / (mL & mL)		$(NH_4)_6Mo_7O_{24}$ / Water (mg) / (mL)		NH_4OH (μL)	Time	Structure
Mo-PDA-PS	15	2	25	2 & 1	100	4	100	8 h	Solid
	15	2	25	2 & 1	100	4	300	8 h	Solid
	15	2	25	2 & 1	100	4	500	8 h	Hollow
	15	2	25	2 & 1	100	4	500	5 min	Solid
	15	2	25	2 & 1	100	4	500	2 h	↓
	15	2	25	2 & 1	100	4	500	8 h	Hollow

Table S2. Physicochemical properties and element compositions of MMo_2C/NCS after carbonization at various temperature (700, 800, and 900 °C)

Carbonization temperature (°C)	Surface area (m^2 g^{-1})	Pore volume (cm^3 g^{-1})	I_G/I_D	N content (atomic%)	Relative ratios of pyridinic-N : graphitic-N
700	165	0.51	0.80	6.9	64% : 36%
800	200	0.55	0.95	5.4	73% : 27%
900	212	0.56	1.09	4.7	77% : 23%

Table S3. Summary of ORR activities of hollow spherical MMo_2C/NCS and recent reported Mo_2C-based and other heteroatom-doped carbon materials in 0.1 M KOH (electrode rotating speed 1600 rpm, the potential is *vs.* RHE).

Catalysts	Mass loading (mg cm^{-2})	Onset potential (V)	Half-wave potential (V)	Electron transfer number (n)	Reference
Hollow spherical MMo_2C/NCS	0.2	0.92	0.83	3.5	This work
Mo_2C-GNR	0.2	0.93	0.81	3.9	[S5]
Mo_2C/NPCNFs	0.4	0.9	0.77	~3.8	[S6]
Hollow Mo_2C–C microspheres	0.4	0.832	0.713	3.2-3.6	[S7]
CoMo carbide/Graphene	0.51	0.894	0.754	3.6	[S8]
Fe-N/C-800	0.079	0.98	~0.82	3.97	[S9]
FeCo-C	0.6	0.91	0.81	4.0	[S10]
Fe-N-Doped Carbon Nanofibers	0.6	0.944	0.824	3.93-3.95	[S11]
N,P-codoped ordered mesoporous carbon	0.3	0.92	0.82	3.5	[S12]
S-doped graphene	N/A	0.88	0.66	3.13	[S13]
Nitrogen-Doped Graphene/Cobalt-Embedded Porous Carbon	0.714	0.94	N/A	3.3	[S14]
Ni_3Fe/N-C sheets Ni_3Fe/N-C	0.13	0.90	0.78	3.75-3.87	[S15]
Carbon-Supported Mn–Co	0.08	0.883	0.803	3.83	[S16]
N-Co-doped Carbon Nanoframes	N/A	0.882	0.809	3.8	[S17]

[S1] J. Tang, J. Liu, C. Li, Y. Li, M. O. Tade, S. Dai and Y. Yamauchi, *Angew. Chem. Int. Ed.*, 2015, **54**, 588-593.

[S2] S. Liu, F. Wang, R. Dong, T. Zhang, J. Zhang , X. Zhuang, Y. Mai and X. Feng, *Adv. Mater.*, 2016, **28**, 8365–8370

[S3] T.-E. Chang, A. Kisliuk, S. M. Rhodes, W. J. Brittain and A. P. Sokolov, *Polymer,* 2006, **47**, 7740-7746.

[S4] D. Mattia, M. P. Rossi, B. M. Kim, G. Korneva, H. H. Bau and Y. Gogotsi, *J. Phys. Chem. B,* 2006, **110***,* 9850-9855.

[S5] X. Fan, Y. Liu, Z. Peng, Z. Zhang, H. Zhou, X. Zhang, B. I. Yakobson, W. A. Goddard III, X. Guo, R. H. Hauge and J. M. Tour, *ACS nano*, 2017, **11**, 384-394.

[S6] H. Wang, C. Sun, Y. Cao, J. Zhu, Y. Chen, J. Guo, J. Zhao, Y. Sun and G. Zou, *Carbon*, 2017, **114***,* 628-634.

[S7] Y. Luo, Z. Wang, Y. Fu, C. Jin, Q. Wei and R. Yang, *J. Mater. Chem. A*, 2016, **4***,* 12583-12590.

[S8] H. Yang, J. Liu, J. Wang, C. K. Poh, W. Zhou, J. Lin and Z. Shen, *Electrochimica Acta*, 2016, **216***,* 246-252.

[S9] W. Niu, L. Li, X. Liu, N. Wang, J. Liu, W. Zhou, Z. Tang and S. Chen, *J. Am. Chem. Soc.,* 2015, **137***,* 5555-5562.

[S10] G. Wu, K. L. More, C. M. Johnston and P. Zelenay, *Science*, 2011, **332***,* 443-447.

[S11] Z.-Y. Wu, X.-X. Xu, B.-C. Hu, H.-W. Liang, Y. Lin, L.-F. Chen and S.-H. Yu, *Angew. Chem. Int. Ed.*, 2015, **54***,* 8179-8183.

[S12] S. Lee, M. Choun, Y. Ye, J. Lee, Y. Mun, E. Kang, J. Hwang, Y.-H. Lee, C.-H. Shin, S.-H. Moon, S.-K. Kim, E. Lee and J. Lee, *Angew. Chem. Int. Ed.,* 2015, **54***,* 9230-9234.

[S13] Z. Ma, S. Dou, A. Shen, L. Tao, L. Dai and S. Wang, *Angew. Chem. Int. Ed.,* 2015, **54***,* 1888-1892.

[S14] Y. Hou, Z. Wen, S. Cui, S. Ci, S. Mao and J. Chen, *Adv. Func. Mater.,* 2015, **25***,* 872-882.

[S15] G. Fu, Z. Cui, Y. Chen, Y. Li, Y. Tang and J. B. Goodenough, *Adv. Energy Mater.,* 2017, **7***,* 1601172.

[S16] X. Yan, Y. Jia, J. Chen, Z. Zhu and X. Yao, *Adv. Mater.,* 2016, **28***,* 8771-8778.

[S17] L. Shang, H. Yu, X. Huang, T. Bian, R. Shi, Y. Zhao, G. I. N. Waterhouse, L.-Z. Wu, C.-H. Tung and T. Zhang, *Adv. Mater.,* 2016, **28***,* 1668-1674.